Statistical Evaluation of Delay and Doppler Spreads in sub-6 GHz and mmWave Vehicular Channels

Faruk Pasic*, Markus Hofer†, Mariam Mussbah*, Herbert Groll*, Thomas Zemen†,
Stefan Schwarz* and Christoph F. Mecklenbräuker*
*Institute of Telecommunications, TU Wien, Vienna, Austria
†AIT Austrian Institute of Technology, Vienna, Austria
faruk.pasic@tuwien.ac.at

Abstract—One of the key research directions to increase the capacity of new radio (NR) vehicle-to-everything (V2X) communication systems is extension of employed frequency bands from sub-6 GHz to millimeter wave (mmWave) range. To investigate different propagation effects between sub-6 GHz and mmWave bands in high-mobility scenarios, one needs to conduct channel measurements in both frequency bands. Using a suitable testbed setup to compare these two bands in a fair manner, we perform channel measurements at center frequencies of 2.55 GHz and 25.5 GHz, velocities of 50 km/h and 100 km/h, and at 126 different spatial positions. Furthermore, we conduct a comparative study of the multi-band propagation based on measurement results. We estimate the power delay profile (PDP) and the Doppler power spectral density (DSD) from a large set of measurements collected in a measurement campaign. Finally, we compare measured wireless channels at the two employed frequency bands in terms of root-mean-square (RMS) delay spread and RMS Doppler spread.

Index Terms—mmWave, sub 6 GHz, 5G, statistical evaluation, vehicular communications, testbed, channel measurements, RMS delay spread, RMS Doppler spread.

I. INTRODUCTION

To increase road safety and improve the traffic flow in urban environments, the next generations of vehicles are expected to support advanced services, such as object detection, risk identification and car platooning [1], [2]. These services require high data transmission rates which cannot be achieved in conventional sub-6 GHz bands. A possible answer to this growing demand for high transmission rates can be found in millimeter wave (mmWave) bands. Thus, developing mmWave communication systems for vehicle-to-everything (V2X) scenarios is attracting increasingly more attention.

There are several works in the literature studying propagation in vehicular scenarios at sub-6 GHz [3]–[7] and at mmWave [8]–[12] bands separately. To learn how propagation and scattering effects change from sub-6 GHz to mmWave bands, comparative measurements over different bands have to be conducted. There are few comparative multi-band analyses in the literature considering statical [13], [14] and drive-by vehicular scenarios [15]–[17].

Statical measurements allow the analysis of the frequency selectivity but not the time selectivity of a vehicular channel. On the other hand, drive-by measurements allow for both time- and frequency-selectivity analysis but pose the problem of antenna placement. Due to mechanical reasons, different antennas for different frequency bands cannot be placed at the same position at the same time. Placing antennas for different frequency bands several centimeters apart leads to a position offset of several wavelengths at mmWave frequencies. This difference in antenna position may result in a different small-scale fading behavior or altered channel statistics.

Contribution: We use a modified version of the testbed setup proposed in [18] to conduct repeatable channel measurements. Our testbed setup allows high-mobility wireless channel measurements with identical transmit and receive antenna positions but at different frequency bands. The measurements have been conducted at the center frequency of 2.55 GHz and 25.5 GHz and transmitter velocity of 50 km/h and 100 km/h at 126 different spatial positions. From a set of collected measurements, we estimate a local scattering function (LSF), followed by the estimation of the power delay profile (PDP) and the Doppler power spectral density (DSD). Based on the obtained PDP and DSD, we perform a comparative statistical analysis between sub-6 GHz and mmWave frequency bands in terms of root-mean-square (RMS) delay spread and RMS Doppler spread.

The rest of the paper is organized as follows. Section II describes our testbed hardware for sub-6 GHz and mmWave channel measurements. The measurement campaign is described in Section III. The evaluation and post-processing of the measured data are explained in Section IV. We discuss obtained results in terms of RMS delay spread and RMS Doppler spread in Section V. Finally, Section VI concludes the paper.

II. MEASUREMENT SETUP

Our testbed setup allows repeatable measurements at different frequency bands in a controlled environment at high velocities of up to 400 km/h. The setup is described in [18] and consists of a moving transmitter and a static receiver. The moving transmitter is based on a rotary unit which rotates an antenna around a central axis at a constant but adjustable velocity [19]. Further, the rotary unit is equipped with a trigger unit and rotary joints. The trigger unit starts the measurement at a precisely defined angle, while the rotary joints feed transmit signals from a signal source to the antenna placed at the end of the rotating arm. The whole rotary unit is placed
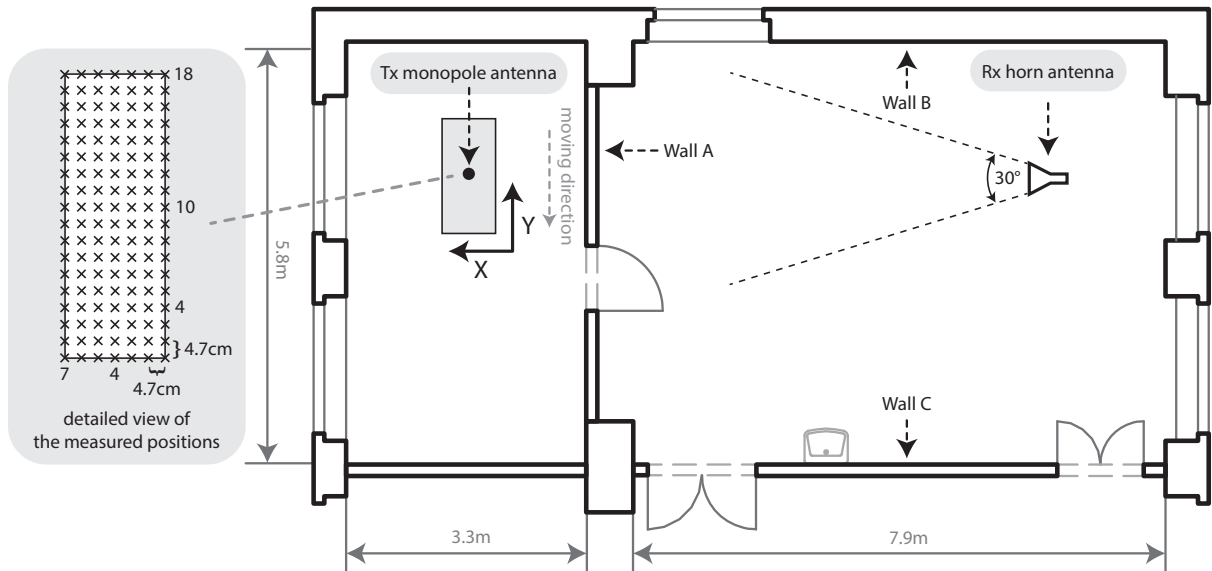
Fig. 1. Measured indoor laboratory environment. The moving transmit antenna and the statical receive antenna are located in neighboring rooms. Detailed view of the measured positions shows the transmit antenna position when passing 0° of the measured arc segment.
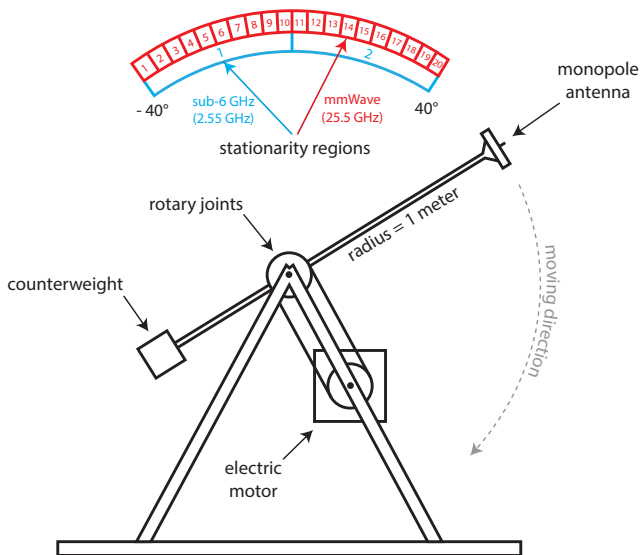

Fig. 2. The rotary unit to perform repeatable high-speed channel measurements at different frequency bands. Blue and red regions are the assumed stationarity regions along the arc segment.

on a sliding board, which can be moved by 33 centimeters along the x-axis and 81 centimeters along the y-axis. This offset of the rotary unit allows for measurements at different spatial transmitter positions. The testbed setup operates in sub-6 GHz and mmWave bands. In the sub-6 GHz case, the radio frequency (RF) signal is directly fed to the antenna at the end of the rotary arm. In the mmWave case, we use a mmWave transmitter [20] placed at the end of the rotary arm to generate the RF signal.

Compared to the previous measurement setup described in [18], we use antennas with similar radiation patterns to improve the comparability of measurements between different frequency bands. Specifically, we use in both bands horn antennas with half-power beamwidth (HPBW) of 30° at the receiver and monopole antennas at the transmitter.

III. MEASUREMENT CAMPAIGN

Using the testbed setup described in Section II, we perform channel-sounding measurements in an indoor environment as shown in Fig. 1. The transmit antenna is placed in a smaller room and is moving with a constant velocity at the rotary unit (see Fig. 2). The receive antenna is placed in a larger room about 7.5 m apart from the transmit antenna and is static on a laboratory table. We conduct measurements at center frequencies of 2.55 GHz and 25.5 GHz, velocities of 50 km/h and 100 km/h, and different spatial positions according to the rectangular grid shown in Fig. 1. Measurement scenarios and corresponding parameters are provided in Tab. I.

To compare measurements at different velocities and different frequency bands in a fair manner, we satisfy two following criteria from [18]. Firstly, the fading environment has to be static. Therefore, we conduct the measurement campaign within 2 hours with no people or moving objects within the room during the measurements. Secondly, the channel measurements have to be performed with the same transmit antenna positions and the same receive antenna position. Therefore, we ensure that the rotating antenna moves along the same trace (arc segment) from −40° to 40° and transmits the same amount of symbols for all measured scenarios. Specifically, we choose a short symbol duration of 1 μs for high-velocity measurements and a long symbol duration of 2 μs for low-velocity measurements (see Tab. I). This allows a fair comparison of the measured wireless channel in terms of fading environment and channel statistics.

TABLE I
CHANNEL SOUNDING PARAMETERS

Parameter	Value			
Bandwidth B [MHz]	100			
Delay Resolution $\Delta\tau$ [ns]	10			
Number of Snapshots N	500			
Symbols per Snapshot N_{sym}	100			
Number of x-axis Positions N_{x}	7			
Number of y-axis Positions N_{y}	18			
Measured Arc Segment	$-40°\ldots 40°$			
	A	**B**	**C**	**D**
Carrier Frequency f_{c} [GHz]	2.55	2.55	25.5	25.5
Wavelength λ [cm]	11.7	11.7	1.17	1.17
Transmitter Velocity v_{Tx} [km/h]	50	100	50	100
Number of Subcarriers K	200	100	200	100
Subcarrier Spacing $\triangle f$ [kHz]	500	1000	500	1000
Symbol Duration t_{s} [μs]	2	1	2	1
Snapshot Duration t_{snap} [μs]	200	100	200	100
Measurement Duration t_{m} [ms]	100	50	100	50
Max. Doppler Shift ν_{max} [Hz]	118.1	236.2	1181	2362
Snapshots per stat. region L	250	250	25	25

We transmit a sequence of 50 000 identical orthogonal frequency-division multiplexing (OFDM) transmit symbols as channel-sounding signal. The transmit symbols are designed using a Zadoff-Chu sequence to keep the peak-to-average power ratio (PAPR) low [21]. At the receiver side, the measurement sequence is grouped into 500 snapshots of 100 symbols each. This grouping is made under the assumption that the wireless channel between the moving antenna and the static receiver is constant in time for the duration of one snapshot. Further, we exploit the first OFDM symbol of each snapshot as a cyclic prefix, discard it, and perform averaging of the remaining 99 symbols to improve the Signal-to-Noise Ratio (SNR) by approximately 20 dB. After OFDM processing, we estimate the wireless channel via least-square estimation for all subcarriers. Finally, we obtain a time-variant channel transfer function (CTF) $\text{H}[n,k]$ for discrete-time (snapshots) $n \in \{-N/2,\ldots,N/2-1\}$ and frequency (subcarriers) $k \in \{-K/2,\ldots,K/2-1\}$.

IV. MEASUREMENT EVALUATION

To analyze the time-frequency dispersion, we characterize the channel by the LSF using the concept from [22]. For each measured scenario, we assume the channel to be locally stationary within a window of approximately 6λ of motion (see Fig. 2) and over the entire frequency range, without further justification. A window of 6λ corresponds to $L = 250$ snapshots for the 2.55 GHz case and $L = 25$ snapshots for the 25.5 GHz case. The time index of each stationarity region is $\eta \in \{1,\ldots,\frac{N}{L}\}$ and corresponds to the center of the stationarity region. To obtain multiple independent spectral

estimates from CTFs, we use the following multitaper based estimator

$$\mathcal{H}_\eta^w[\tau,\nu] = \sum_{n=-\frac{N}{2}}^{\frac{N}{2}-1} \sum_{k=-\frac{K}{2}}^{\frac{K}{2}-1} \text{H}[n+\eta L, k] \cdot \text{G}^w[n,k,\tau,\nu], \quad (1)$$

where

$$\text{G}^w[n,k,\tau,\nu] = \text{G}[n,k]\, e^{j2\pi(\nu n - \tau k)} \quad (2)$$

is a separable taper using the two-dimensional discrete prolate spheroidal sequences in time and frequency [23]. In (1) and (2), $\nu \in \{-L/2,\ldots,L/2-1\}$ denotes the Doppler index and $\tau \in \{0,\ldots,K-1\}$ represents the delay index. The delay and Doppler shift resolutions are given by $\Delta\tau = 1/B$ and $\Delta\nu = 1/(Lt_{\text{snap}})$. The number of tapers in time and frequency domain are set to $I = 3$ and $J = 3$, respectively [8]. The LSFs of each window are then averaged to produce an average LSFs

$$\text{S}_\eta[\tau,\nu] = \frac{1}{IJ} \sum_{w=0}^{IJ-1} \left|\mathcal{H}_\eta^w[\tau,\nu]\right|^2. \quad (3)$$

After that, we calculate the PDP and DSD as the expectation of the LSF over the Doppler domain or the delay domain, respectively:

$$\text{P}_\eta[\tau] = \frac{1}{L} \sum_{\forall\nu} \text{S}_\eta[\tau,\nu] \quad (4)$$

$$\text{D}_\eta[\nu] = \frac{1}{K} \sum_{\forall\tau} \text{S}_\eta[\tau,\nu]. \quad (5)$$

To allow for better comparability between different frequency bands and different velocities, we perform the following adjustments:

- We normalize the power of $\text{P}_\eta[\tau]$ and $\text{D}_\eta[\nu]$ such that 0 dB is the greatest occurring value.
- We define the dynamic range (DR) as the difference between maximum power and noise floor and consider the values outside the DR as a corresponding noise floor. Since we have different DRs for different frequency bands, we choose the DR to be the smallest one to maintain a fair comparison.
- We define the normalized Doppler shift ν_{N} as

$$\nu_{\text{N}} = \frac{\nu}{f_{\text{c}} v_{\text{Tx}}} \left[\frac{\text{Hz}}{\text{Hz}\frac{\text{m}}{\text{s}}} = \frac{\text{s}}{\text{m}}\right], \quad (6)$$

where f_{c} is the center frequency, v_{Tx} is the transmit antenna velocity and ν is the Doppler shift. This way, the $\text{D}_\eta[\nu]$ is confined to same interval of ν_{N} for all measured scenarios.

As an illustrative example, the PDP and normalized DSD averaged over stationarity regions η for position 1 on the x-axis and position 5 on the y-axis are shown in Fig. 3.

Further, we calculate the RMS delay spread σ_η^τ and normalized RMS Doppler spread $\sigma_\eta^{\nu_{\text{N}}}$ as second-order moments of $\text{P}_\eta[\tau]$ and $\text{D}_\eta[\nu_{\text{N}}]$, respectively. The RMS delay and normalized RMS Doppler spreads are directly related to the coherence bandwidth and coherence time of the channel,
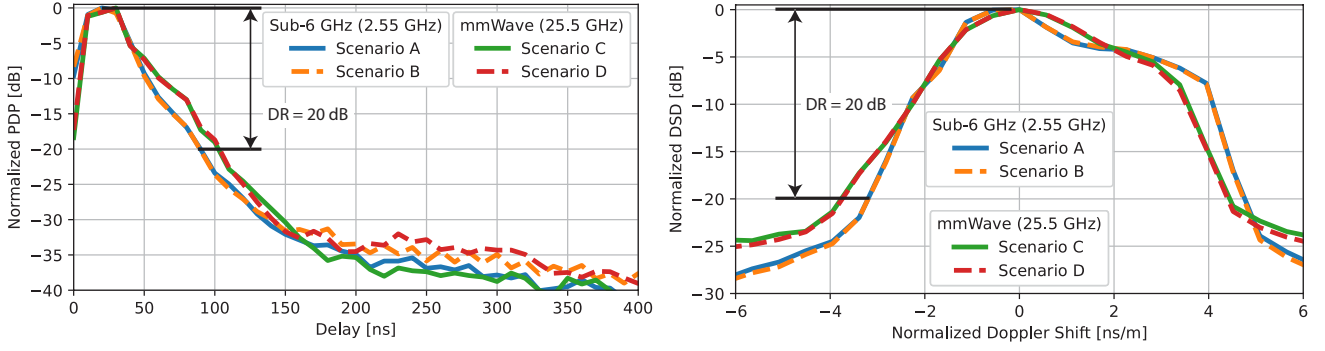
Fig. 3. Normalized PDP and normalized DSD averaged over stationarity regions η at spatial position $(x, y) = (1, 5)$.
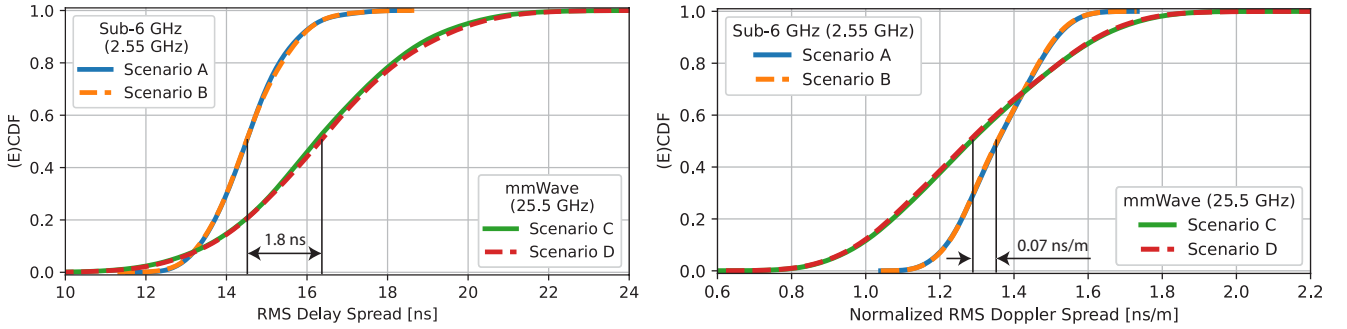

Fig. 4. RMS Delay Spread and normalized RMS Doppler Spread are almost invariant with regard to the transmitter velocity.

which indicate the rate of change of the channel in frequency and time, respectively [24]. The RMS delay spread is given by

$$
\sigma_\eta^\tau = \sqrt{\frac{\sum\limits_{\forall \tau} \tau^2 P_\eta[\tau]}{\sum\limits_{\forall \tau} P_\eta[\tau]} - \left(\frac{\sum\limits_{\forall \tau} \tau P_\eta[\tau]}{\sum\limits_{\forall \tau} P_\eta[\tau]}\right)^2}
\tag{7}
$$

and the normalized RMS Doppler spread is given by

$$
\sigma_\eta^{\nu_{\mathrm{N}}} = \sqrt{\frac{\sum\limits_{\forall \nu_{\mathrm{N}}} \nu_{\mathrm{N}}^2 D_\eta[\nu_{\mathrm{N}}]}{\sum\limits_{\forall \nu_{\mathrm{N}}} D_\eta[\nu_{\mathrm{N}}]} - \left(\frac{\sum\limits_{\forall \nu_{\mathrm{N}}} \nu_{\mathrm{N}} D_\eta[\nu_{\mathrm{N}}]}{\sum\limits_{\forall \nu_{\mathrm{N}}} D_\eta[\nu_{\mathrm{N}}]}\right)^2}.
\tag{8}
$$

V. RESULTS AND DISCUSSION

We perform the statistical evaluation of the channel spreads by calculating σ_η^τ and $\sigma_\eta^{\nu_{\mathrm{N}}}$ for each position x and y according to the rectangular grid from Fig. 1, where $x \in \{1, \ldots, N_{\mathrm{x}}\}$ and $y \in \{1, \ldots, N_{\mathrm{y}}\}$. We plot in Fig. 4 the cumulative distribution function (CDF) of the RMS delay spread $\sigma_{\eta,\mathrm{x},\mathrm{y}}^\tau$ and normalized RMS Doppler spread $\sigma_{\eta,\mathrm{x},\mathrm{y}}^{\nu_{\mathrm{N}}}$ for all stationarity regions η and spatial positions x and y. The obtained mean and standard deviation values for the different scenarios are summarized in Tab. II.

One can observe a higher standard deviation for the mmWave scenarios compared to the sub-6 GHz scenarios.

This occurs due to the following phenomena. Firstly, for 25.5 GHz the stationarity region of 6λ is spatially smaller. By performing measurements over the same arc segment from -40° to 40°, we obtain more independent realizations of mmWave channels than sub-6 GHz channels, as shown in Fig. 2. Secondly, the distance of 4.7 cm between different spatial positions (see Fig. 1) corresponds to $0.4\,\lambda$ for the sub-6 GHz scenarios and $4\,\lambda$ for the mmWave scenarios.

Furthermore, it can be observed that for the mmWave band, the mean RMS delay spread is larger by about 1.8 ns (12%). However, this difference is negligible on a large scale and should not significantly impact the system design. The mean values of the normalized RMS Doppler spread are similar for different frequency bands as well, with the fact that the sub-6 GHz scenarios have a slightly higher value by about 0.07 ns/m (5%) compared to the mmWave scenarios. Due to the spatial filtering by the receive antennas, the mean values are 40% and 38% less than the maximum normalized RMS Doppler shift ($\nu_{\mathrm{N,max}} = 3.33$ ns/m) for the sub-6 GHz and mmWave scenarios, respectively.

One can notice that both spreads are almost invariant with regard to the transmitter's velocity, although the measurements were performed at different times. In other words, there is a significant agreement between different scenarios within the same frequency band. The largest mean difference between the low-velocity and high-velocity scenarios within the same

|		Region 1 + Region 2				Region 1				Region 2			
		$\sigma^{\tau}_{\eta,\mathrm{x,y}}$ [ns]		$\sigma^{\nu_N}_{\eta,\mathrm{x,y}}$ [ns/m]		$\sigma^{\tau}_{\eta,\mathrm{x,y}}$ [ns]		$\sigma^{\nu_N}_{\eta,\mathrm{x,y}}$ [ns/m]		$\sigma^{\tau}_{\eta,\mathrm{x,y}}$ [ns]		$\sigma^{\nu_N}_{\eta,\mathrm{x,y}}$ [ns/m]	
		Mean	Std.	Mean	Std.	Mean	Std.	Mean	Std.	Mean	Std.	Mean	Std.
sub-6 GHz	Scenario A	14.54	0.91	1.36	0.11	14.07	1.12	1.26	0.09	15.00	1.06	1.46	0.18
(2.55 GHz)	Scenario B	14.54	0.93	1.36	0.10	14.10	1.14	1.26	0.09	14.98	0.99	1.46	0.18
mmWave	Scenario C	16.28	2.14	1.30	0.24	15.73	2.13	1.19	0.20	16.83	2.01	1.41	0.22
(25.5 GHz)	Scenario D	16.37	2.18	1.29	0.24	15.81	2.18	1.19	0.20	16.92	2.04	1.40	0.23
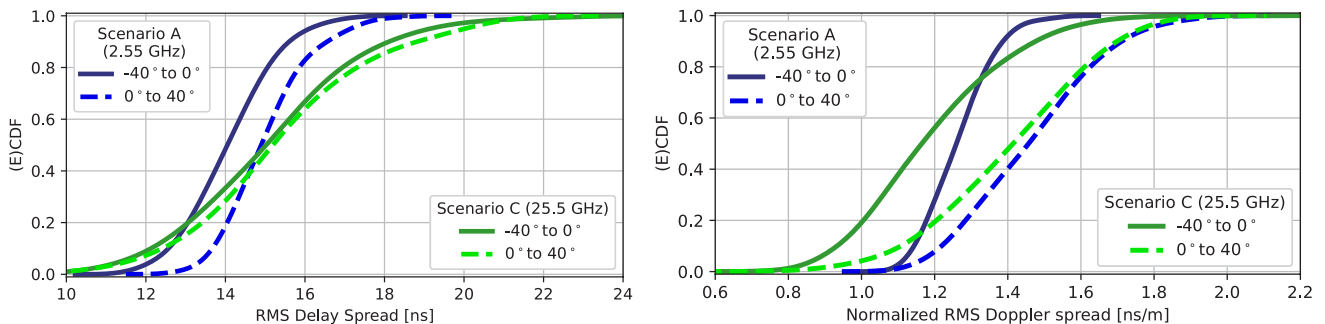
Fig. 5. As the transmit antenna approaches the door, many unblocked multipath components pass into the neighboring room with the receiver, which results in increased RMS delay spread and normalized RMS Doppler spread.

frequency band is around 0.7%. Thereby, we confirm the accuracy of our testbed for repeatable measurements proposed in [20], since such a deviation between the low-velocity and high-velocity scenarios is negligible on a large scale.

To characterize the channel variation over different angular transmit antenna positions within the rotary unit, we cluster the RMS delay spreads and normalized RMS Doppler spreads into the two following regions,

- region 1 (antenna moving upwards from -40° to 0°)
- region 2 (antenna moving downwards from 0° to 40°)

and plot corresponding CDFs (see Fig. 5). Mean and standard deviation values for both regions are summarized in Tab. II.

In region 1, the strongest path of the transmitted signal reaches the receiver by passing through wall A, while dominant reflections originate from wall B (see Fig. 1). Due to the blockage of the direct path from wall A, signal components arrive at the receiver significantly attenuated. Furthermore, due to the proximity of the transmit antenna to wall B, associated multipath components arrive within a short delay window. Therefore, region 1 scenario poses lower values of both RMS delay spread and normalized RMS Doppler spread.

In region 2, the transmit antenna moves away from wall B and approaches the door. Compared to region 1 scenario, many unblocked multipath components pass into the neighboring room, where the receiver is located. Due to possible wave diffraction around the door and longer delays for multipath

components associated with bounces at wall C, the mean values of the RMS delay spread and normalized RMS Doppler spread increase by around 7% and 16%, respectively.

VI. CONCLUSION

We perform high-mobility wireless channel measurements enabling a direct comparison of propagation at sub-6 GHz and mmWave bands at different spatial positions. Our testbed to compare different frequency bands in a fair manner works correctly and is able to reproduce an experiment with minor uncertainties. The measured results show small differences on the RMS delay spread and normalized RMS Doppler spread, thereby offering almost the same propagation conditions at different frequency bands. The antenna directivity impacts the normalized RMS Doppler spread to a great extent. The angular position of the moving transmit antenna within the rotary unit influences the channel parameters.

References

[1] M. Giordani, A. Zanella, and M. Zorzi, "Millimeter wave communication in vehicular networks: Challenges and opportunities," in *2017 6th International Conference on Modern Circuits and Systems Technologies (MOCAST)*, 2017.

[2] A. L. Gratzer, A. Schirrer, E. Thonhofer, F. Pasic, S. Jakubek, and C. F. Mecklenbräuker, "Short-Term Collision Estimation by Stochastic Predictions in Multi-Agent Intersection Traffic," in *Proc. of the International Conference on Electrical, Computer and Energy Technologies (ICECET 2022)*, 2022.

[3] V. Shivaldova, A. Paier, D. Smely, and C. F. Mecklenbräuker, "On Roadside Unit Antenna Measurements for Vehicle-to-Infrastructure Communications," in *2012 IEEE 23rd International Symposium on Personal, Indoor and Mobile Radio Communications - (PIMRC)*, 2012, pp. 1295–1299.

[4] F. Pasic, S. Pratschner, R. Langwieser, and C. F. Mecklenbräuker, "High-Mobility Wireless Channel Measurements at 5.9 GHz in an Urban Environment," in *2022 International Balkan Conference on Communications and Networking (BalkanCom)*, 2022, pp. 100–104.

[5] J. Kunisch and J. Pamp, "Wideband Car-to-Car Radio Channel Measurements and Model at 5.9 GHz," in *2008 IEEE 68th Vehicular Technology Conference*, 2008.

[6] Z. Su, L. Liu, Y. Fan, S. Dong, L. Zhang, J. Qiu, and X. Lin, "Measurements and Characteristics for Vehicle to Everything Channel in Tunnel Scenario at 5.9 GHz," in *2021 7th International Conference on Computer and Communications (ICCC)*, 2021, pp. 230–234.

[7] H. Fernández, V. M. Rodrigo-Peñarrocha, L. Rubio, and J. Reig, "Path Loss Characterization in Vehicular Environments under LOS and NLOS Conditions at 5.9 GHz," in *The 8th European Conference on Antennas and Propagation (EuCAP 2014)*, 2014, pp. 3044–3048.

[8] E. Zöchmann, M. Hofer, M. Lerch, S. Pratschner, L. Bernadó, J. Blumenstein, S. Caban, S. Sangodoyin, H. Groll, T. Zemen, A. Prokeš, M. Rupp, A. F. Molisch, and C. F. Mecklenbräuker, "Position-specific statistics of 60 GHz vehicular channels during overtaking," *IEEE Access*, vol. 7, pp. 14 216–14 232, 2019.

[9] E. Zöchmann, C. F. Mecklenbräuker, M. Lerch, S. Pratschner, M. Hofer, D. Löschenbrand, J. Blumenstein, S. Sangodoyin, G. Artner, S. Caban, T. Zemen, A. Prokeš, M. Rupp, and A. F. Molisch, "Measured delay and Doppler profiles of overtaking vehicles at 60 GHz," in *12th European Conference on Antennas and Propagation (EuCAP 2018)*, 2018.

[10] H. Groll, E. Zöchmann, S. Pratschner, M. Lerch, D. Schützenhöfer, M. Hofer, J. Blumenstein, S. Sangodoyin, T. Zemen, A. Prokeš, A. F. Molisch, and S. Caban, "Sparsity in the Delay-Doppler Domain for Measured 60 GHz Vehicle-to-Infrastructure Communication Channels," in *2019 IEEE International Conference on Communications Workshops (ICC Workshops)*, 2019.

[11] J. Park, J. Lee, K. Kim, and M. Kim, "28-GHz High-Speed Train Measurements and Propagation Characteristics Analysis," in *2020 14th European Conference on Antennas and Propagation (EuCAP)*, 2020.

[12] D. He, B. Ai, K. Guan, Z. Zhong, B. Hui, J. Kim, H. Chung, and I. Kim, "Channel Measurement, Simulation, and Analysis for High-Speed Railway Communications in 5G Millimeter-Wave Band," *IEEE Transactions on Intelligent Transportation Systems*, vol. 19, no. 10, pp. 3144–3158, 2018.

[13] D. Dupleich, R. Müller, M. Landmann, E.-A. Shinwasusin, K. Saito, J.-I. Takada, J. Luo, R. Thomä, and G. Del Galdo, "Multi-band propagation and radio channel characterization in street canyon scenarios for 5G and beyond," *IEEE Access*, vol. 7, pp. 160 385–160 396, 2019.

[14] M. Boban, D. Dupleich, N. Iqbal, J. Luo, C. Schneider, R. Müller, Z. Yu, D. Steer, T. Jämsä, J. Li, and R. S. Thomä, "Multi-Band Vehicle-to-Vehicle Channel Characterization in the Presence of Vehicle Blockage," *IEEE Access*, vol. 7, pp. 9724–9735, 2019.

[15] M. Hofer, D. Löschenbrand, J. Blumenstein, H. Groll, S. Zelenbaba, B. Rainer, L. Bernadó, J. Vychodil, T. Mikulasek, E. Zöchmann, S. Sangodoyin, H. Hammoud, B. Schrenk, R. Langwieser, S. Pratschner, A. Prokes, A. F. Molisch, C. F. Mecklenbräuker, and T. Zemen, "Wireless Vehicular Multiband Measurements in Centimeterwave and Millimeterwave Bands," in *2021 IEEE 32nd Annual International Symposium on Personal, Indoor and Mobile Radio Communications (PIMRC)*, 2021, pp. 836–841.

[16] M. Hofer, D. Löschenbrand, S. Zelenbaba, A. Dakić, B. Rainer, and T. Zemen, "Wireless 3 GHz and 30 GHz Vehicle-to-Vehicle Measurements in an Urban Street Scenario," in *2022 IEEE 96th Vehicular Technology Conference (VTC2022-Fall)*, 2022. [Online]. Available: http://thomaszemen.org/papers/Hofer22-VTCFall-paper.pdf

[17] H. Wang, X. Yin, J. Rodríguez-Piñeiro, J. Lee, and M. Kim, "Shadowing and Multipath-Fading Statistics at 2.4 GHz and 39 GHz in Vehicle-to-Vehicle Scenarios," in *2020 14th European Conference on Antennas and Propagation (EuCAP)*, 2020.

[18] F. Pasic, D. Schützenhöfer, E. Jirousek, R. Langwieser, H. Groll, S. Pratschner, S. Caban, S. Schwarz, and M. Rupp, "Comparison of Sub 6 GHz and mmWave Wireless Channel Measurements at High Speeds," in *16th European Conference on Antennas and Propagation (EuCAP 2022)*, 2022.

[19] S. Caban, J. Rodas, and J. A. García-Naya, "A methodology for repeatable, off-line, closed-loop wireless communication system measurements at very high velocities of up to 560 km/h," in *2011 IEEE International Instrumentation and Measurement Technology Conference*, 2011.

[20] F. Pasic, S. Pratschner, R. Langwieser, D. Schützenhöfer, E. Jirousek, H. Groll, S. Caban, and M. Rupp, "Sub 6 GHz versus mmWave Measurements in a Controlled High-Mobility Environment," in *WSA 2021; 25th International ITG Workshop on Smart Antennas*, 2021.

[21] B.-J. Choi, E.-L. Kuan, and L. Hanzo, "Crest-factor study of MC-CDMA and OFDM," in *50th Vehicular Technology Conference*, vol. 1, 1999.

[22] L. Bernadó, T. Zemen, F. Tufvesson, A. F. Molisch, and C. F. Mecklenbräuker, "Delay and Doppler Spreads of Nonstationary Vehicular Channels for Safety-Relevant Scenarios," *IEEE Transactions on Vehicular Technology*, vol. 63, no. 1, 2014.

[23] D. Slepian, "Prolate spheroidal wave functions, fourier analysis, and uncertainty — v: the discrete case," *The Bell System Technical Journal*, vol. 57, no. 5, pp. 1371–1430, 1978.

[24] A. F. Molisch and M. Steinbauer, "Condensed parameters for characterizing wideband mobile radio channels," *International Journal of Wireless Information Networks*, vol. 6, no. 3, pp. 133–154, 1999.